AIAA JOURNAL
Vol. 41, No. 10, October 2003

Laser Energy Deposition in Quiescent Air

H. Yan*
Rutgers University, Piscataway, New Jersey 08854-8058
R. Adelgren†
U.S. Air Force Test Pilot School, Edwards Air Force Base, California 93524-6485
M. Boguszko‡
Rutgers University, Piscataway, New Jersey 08854-8058
G. Elliott§
University of Illinois at Urbana–Champaign, Urbana, Illinois 61801
and
D. Knight¶
Rutgers University, Piscataway, New Jersey 08854-8058

Laser energy deposition in quiescent air has been studied experimentally and numerically. The study is focused on the gasdynamic effects of the laser energy spot on the flow structure. A Gaussian profile for initial temperature distribution is proposed to model the energy spot assuming the density is initially uniform. A filtered Rayleigh scattering technique has been used for obtaining the experimental results. These consisted of flow visualization of the blast wave, and simultaneous pressure, temperature, and velocity measurements. Good agreement has been achieved between numerical and experimental results for shock radius vs time. The comparison of computed and experimental density, pressure, temperature, and velocity outside the laser spot show good agreement as well.

Nomenclature

a_∞	=	ambient speed of sound
B	=	optics calibration constant
C	=	constant dark level
$\hat{\boldsymbol{k}}_0$	=	observed light wave unit vector
$\hat{\boldsymbol{k}}_L$	=	incident light wave unit vector
$l(\nu)$	=	laser spectral distribution
Mo	=	molecular mass
M_s	=	shock Mach number
Pr	=	Prandtl number
p	=	pressure
Q	=	optics calibration constant
R	=	gas constant
R_0	=	focal radius
r	=	Rayleigh scattering (RS) distribution, radius
r_0	=	radius
S	=	the grayscale value collected at a particular pixel of the image
T	=	temperature
$t(\nu)$	=	absorption profile
$\boldsymbol{V}$	=	flow velocity vector
V_0	=	focal volume
V_s	=	shock velocity
x	=	nondimensional frequency in RS
y	=	ratio of collisional frequency to the acoustic spatial frequency in RS
α_R	=	Rosseland mean absorption coefficient
ΔT	=	temperature variation due to energy addition
ΔT_0	=	peak temperature variation due to energy addition
$\Delta\nu_D$	=	Doppler shift
ϵ	=	absorption coefficient
κ	=	constant thermal conductivity
λ	=	wavelength of incident light
μ	=	dynamic viscosity
ν	=	frequency
ν_0	=	incoming light frequency
ρ	=	density
σ_s	=	Stefan–Boltzmann constant, 5.67×10^{-8} W/K^{4}m^2
θ	=	angle between the incident and scattered wave vectors

Subscript

∞	=	ambient value

Received 31 December 2002; revision received 5 June 2003; accepted for publication 11 June 2003.

*Research Assistant Professor, Department of Mechanical and Aerospace Engineering, 98 Brett Road. Senior Member AIAA.
†Major. Member AIAA.
‡Graduate Student, Department of Mechanical and Aerospace Engineering, 98 Brett Road. Student Member AIAA.
§Associate Professor, Department of Aeronautical and Astronautical Engineering, 306 Talbot Laboratory, 104 South Wright Street. Associate Fellow AIAA.
¶Professor, Department of Mechanical and Aerospace Engineering, 98 Brett Road. Associate Fellow AIAA.

Introduction

LASER-INDUCED breakdown in air has been studied since its discovery in 1963.[1] The breakdown is described by four successive stages. Figure 1 illustrates these four stages: 1) the initial release of electrons due to multiphoton collision with the gas molecule, 2) ionization of the gas in the focal region by the cascade release of electrons, 3) formation of the plasma, and 4) formation of the blast wave due to the absorption of laser energy by the plasma and the propagation of the blast wave into the surrounding gas. A primary observation obtained from experiments (Refs. 2 and 3; Adelgren, R., Boguszko, M., and Elliott, G., Rutgers University, Oct. 2001, private communication) is the propagation of the blast wave and the formation of a vortex ring in the focal region due to the asymmetric shape of the plasma region.

Many analytical and numerical models[2,4–15] have been investigated to better understand the essential features of this phenomenon. Similarity laws proposed by Taylor[4] and von Neumann[7] accurately describe the motion of the blast wave at its early stage when it remains strong. Sedov[6] independently derived the same similarity laws as Taylor. Bach and Lee[16] proposed an approximation to describe weak blast waves based on the assumption of a power-law

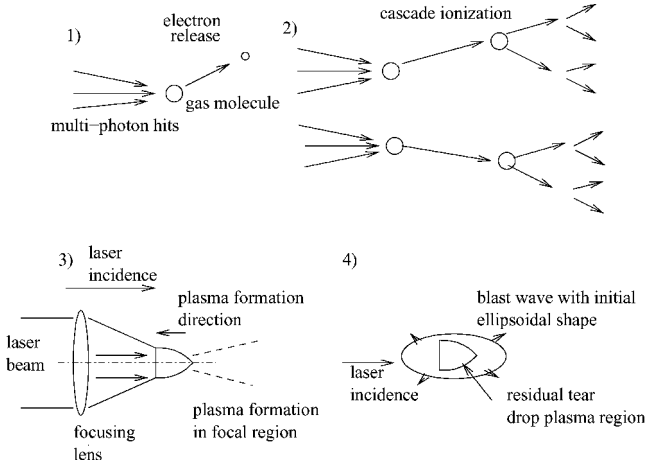

Fig. 1 Formation of laser spot.

density profile behind them. Brode[5] performed a numerical simulation of spherical blast waves using two types of initial conditions: a point source and an isothermal sphere. It is noted that the ideal gas assumption is reasonably valid in air for shock pressures less than 10 atm. Svetsov et al.[2] experimentally and numerically studied the fluid motion due to a laser discharge and the results exhibited a vortex ring due to an initial asymmetry. Steiner et al.[12] presented a real gas model simulation with a self-similar strong shock solution as the initial condition. The laser energy release was taken as a linear function of time. The shock radii of the real gas and the perfect gas solution only slightly differ in contrast to the classical point explosion with a sudden release of a fixed amount of energy. Jiang et al.[11] performed an experimental and numerical simulation of a microblast wave with the initial condition described by the similarity law.[4] Recently, Dors[13] presented a computational model that takes into account the asymmetry of the laser energy deposition as well as ionization and dissociation effects on fluid properties with assumed initial conditions taken upon termination of the laser pulse. Liang et al.[14] demonstrated that there were three outward-moving weaker shock waves behind the main shock in the propagation of a weak spherical blast wave, created by rupture of a high-pressure isothermal sphere.

The present work studies the gasdynamic effects of the laser energy deposition on the flow structure. The comparisons between experimental and numerical simulation are made to validate the proposed initial condition for the laser energy spot. This study is also verifies a computational model that will be used in future studies on the effect of energy deposition on compressible flows.

Filtered Rayleigh Scattering

Flow visualization of the blast wave, created from the laser-induced breakdown in quiescent air, was obtained by a Rayleigh scattering (RS) technique.[17–19] RS is defined as a scattering process for which the interacting particle is less than one-tenth of the wavelength of the incident light. For visible light, scattering that falls in the Rayleigh range is due to the air molecules[20] that can be utilized for flow measurements without the need for any artificial seeding.

The intensity of the RS is a function of the number of scatterers per unit volume, which is proportional to the density of the flow. The RS spectral distribution is a function of the flow velocity, pressure, and temperature.[21]

Considering a unit volume of air and a monochromatic irradiating light, the observed RS profile has a finite spectral distribution about the frequency of the incoming light. This is due to the fact that the molecular random velocities, which are proportional to the gas temperature, produce a Doppler shift in frequency that manifests macroscopically as a broadening of the spectrum.[22] Therefore, the broadening is proportional to the flow temperature. The profile can be parameterized by two nondimensional quantities, namely, the nondimensional frequency x and a parameter y that can be interpreted as the ratio of collisional frequency to the acoustic spatial

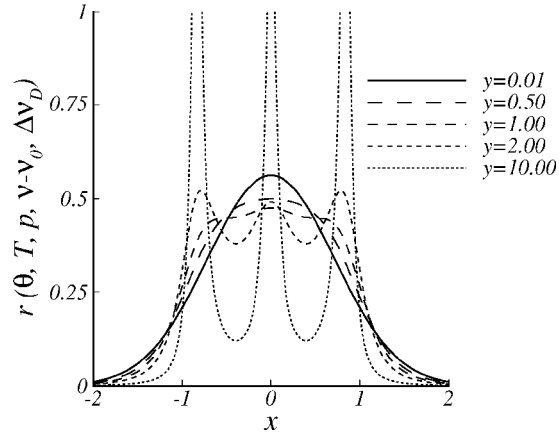

Fig. 2 Rayleigh scattering distribution for various y values.

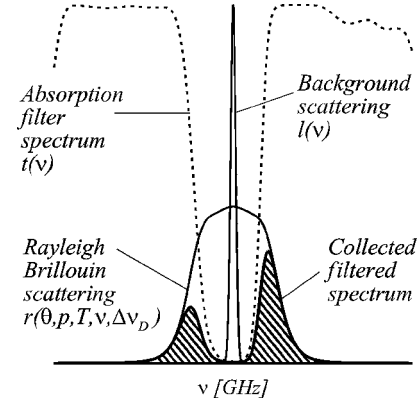

Fig. 3 Scheme of overlapping of scattering and absorption band.

frequency[23] (shown in Fig. 2):

$$y = \frac{\lambda p}{4\pi\mu \sin(\theta/2)}\sqrt{\frac{Mo}{2\sigma_s T}} \tag{1}$$

$$x = \frac{\lambda|\nu - \nu_0|}{2\sin(\theta/2)}\sqrt{\frac{Mo}{2\sigma_s T}} \tag{2}$$

The whole RS profile can also be Doppler shifted in frequency due to the bulk velocity of the flow with respect to the laboratory frame of reference according to

$$\Delta\nu_D = (1/\lambda)\boldsymbol{V}(\hat{k}_0 - \hat{k}_L) \tag{3}$$

In general, the detecting devices, such as cameras or photodiodes, are insensitive to frequency; they only measure total energy or power.[21] To resolve the frequency information and make the thermodynamic property measurements possible, a filter is used. In this experiment, the filter consists of a glass cell filled with molecular iodine that has absorption lines within the tuning range of our 532-nm Nd:YAG tunable laser.

The method is based on tuning the laser across one of these absorption lines, provided that 1) it has sharp cutoff edges, 2) its absorption band is wider than the laser bandwidth, 3) it has a large extinction ratio, and 4) it is isolated from other absorption bands.[22] By placing the filter in front of the detector the signal collected is going to be the convolution of the RS and the absorption profile[21] (Fig. 3):

$$S(\nu_0 + \Delta\nu_D, p, T) = Q\rho \int t(\nu) r(\nu - \nu_0 - \Delta\nu_D, p, T)\,\mathrm{d}\nu$$

$$+ B \int t(\nu) l(\nu)\,\mathrm{d}\nu + C \tag{4}$$

As mentioned, the detector is only sensitive to energy or power, integrating the contributions over the frequency domain, which is

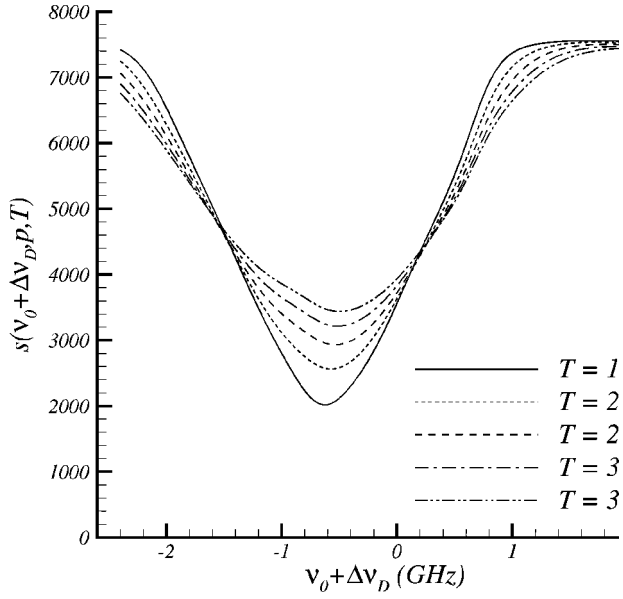

Fig. 4 Grayscale as a function of laser frequency.

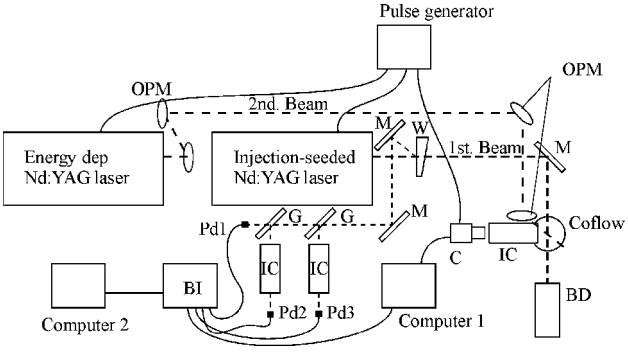

Fig. 5 Experimental arrangement: M, mirror; W, wedge; OPM, off-plane mirror; G, partially reflecting mirror; IC, iodine cell; BI, boxcar integrator; Pd, photodiode; and BD, beam dump.

represented by the area under the solid line in Fig. 3. The collected intensity is due to the molecular RS and the background reflections. The latter have approximately the same spectral linewidth as the laser. The first term of the equation represents the filtered RS and the second term the background scattering.

As the laser is tuned in and out of the absorption band the intensity recorded by the detector varies, producing a curve of grayscale as a function of laser frequency shown in Fig. 4. Using a curve-fitting routine the values of p, T, and $\Delta\nu_D$ are found by iteration. Once $\Delta\nu_D$ is found, a velocity component can be computed by Eq. (3).

Experimental Apparatus

The arrangement for this experiment included two Nd:YAG lasers with an output wavelength of 532 nm. Figure 5 shows the schematic of the experimental arrangement. One of them was tunable in frequency with a power of approximately 500 mJ and was used to create a laser sheet that illuminated the test section. The second laser, with a power of about 180 mJ, was directed to the test section and focused down to a small focal volume to produce an energy discharge (10-ns duration) on the plane of the laser sheet. A Princeton Instruments intensified charge-coupled device (ICCD) camera was placed at 90 deg with respect to the sheet imaging the region of interest. The three elements were controlled by a Stanford Research Systems pulse generator with a frequency of 10 Hz. An iodine cell calibrated at 50°C was placed before the camera to serve as a filter. A Dell Pentium IV personal computer, labeled Computer 1 in Fig. 5, was used to collect the images taken by the camera. The ICCD was also connected via a Princeton Instruments boxcar integrator to a Gateway Pentium III personal computer (Computer 2). The function

Table 1 Test conditions

Parameter	Value
Pressure for quiescent air p_s	0.101 MPa
Temperature for quiescent air T_s	293 K
Laser perturbation focal volume V_0	3 mm^3
Laser beam incidence energy for quiescent air E	108, 112, and 145 mJ/pulse

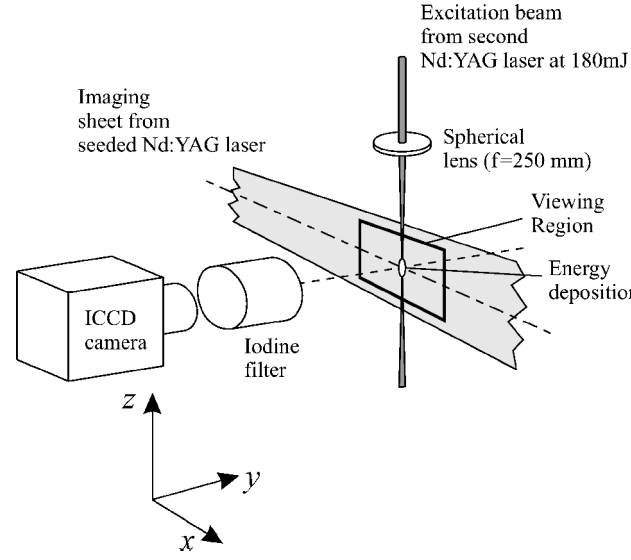

Fig. 6 Test section detail.

of this personal computer was to control the seeding bias voltage of the tunable laser to obtain the desired wavelength.

To accurately monitor the laser frequency, a frequency monitor system was installed on the side of the seeded laser. Using an optical wedge interposed in the path of the first beam a backreflection of about 5% of the total energy is obtained. This backreflection was then directed with two mirrors to a set of photodiodes. One photodiode (Pd1), with no iodine cell in front, monitors the intensity of the laser and the other two (Pd2, Pd3) monitor how much light is being absorbed by the iodine. Because the absorption frequencies are fixed the frequencies at which the images are taken can be accurately monitored.

In Fig. 6 the test section is shown in more detail. Particle scattering due to ambient dust was kept out of the field of view by a very low speed coflow moving from bottom to top. The coflow was slow enough that its influence on the flow of interest was negligible.

The test conditions for the quiescent air case are listed in Table 1.

Numerical Methodology

A one-dimensional time-dependent simulation was performed in the spherical polar coordinate system. Real gas effects are not included. The compressible Navier–Stokes equations in the spherical polar coordinate system can be written as follows:

$$\frac{\partial\rho}{\partial t}+\frac{\partial(\rho v_r)}{\partial r}+\frac{2\rho v_r}{r}=0 \tag{5}$$

$$\frac{\partial\rho v_r}{\partial t}+\frac{\partial\left(\rho v_r^2+p\right)}{\partial r}+\frac{2\rho v_r^2}{r}=\frac{4}{3}\frac{\partial}{\partial r}\left[\mu\left(\frac{\partial v_r}{\partial r}-\frac{v_r}{r}\right)\right]+\frac{4\mu}{r}\left(\frac{\partial v_r}{\partial r}-\frac{v_r}{r}\right) \tag{6}$$

$$\frac{\partial\rho e}{\partial t}+\frac{\partial(\rho e v_r+p v_r)}{\partial r}+\frac{2(\rho e v_r+p v_r)}{r}=\frac{4}{3}\frac{\partial}{\partial r}\left[\mu v_r\left(\frac{\partial v_r}{\partial r}-\frac{v_r}{r}\right)\right]+\frac{8}{3}\mu\frac{v_r}{r}\left(\frac{\partial v_r}{\partial r}-\frac{v_r}{r}\right)+\frac{\partial}{\partial r}\left(\kappa_e\frac{\partial T}{\partial r}\right)+\frac{2}{r}\kappa_e\frac{\partial T}{\partial r} \tag{7}$$

The state equation of ideal gas is

$$p = \rho RT \tag{8}$$

where

$$\kappa_e = \kappa + (16/3)(\sigma_s/\alpha_R)T^3 \tag{9}$$

The dynamic viscosity μ using Sutherland's law is calculated as follows:

$$\mu = \mu_{\text{ref}}\left(\frac{T}{T_{\text{ref}}}\right)^{\frac{3}{2}}\frac{T_{\text{ref}} + 110.4}{T + 110.4} \tag{10}$$

For air, $\mu_{\text{ref}} = 1.71 \times 10^{-5}$ kg/(m · s) at $T_{\text{ref}} = 273$ K. The constant thermal conductivity κ is chosen to keep $Pr = 0.89$, in which μ is computed at $T = 293$ K using Eq. (10). The computed flowfield outside the initial energy deposition region was found to be insensitive to the Rosseland mean absorption coefficient α_R ranging from 1 to 10^6 m^{-1}.

The flux-corrected transport algorithm[24] is used and the second-order Godunov method is applied to compute the inviscid fluxes. The two-stage Runge–Kutta method is utilized for the time integration. The first- and second-order MUSCL scheme[25] is used for the reconstruction of the flow variables at the interfaces of the adjacent cells. The algorithm is second-order accurate in space and time.

Results

Flow Visualization

Filtered RS was used to visualize the flow at different time delays from the laser pulse. The asymmetric formation of the laser deposition region leads to an initial ellipsoidal blast wave and then a subsequent vortex ring formation at later times (Fig. 7). The laser pulse is incident from above in Fig. 7. In the early stages of the formation process, the plasma forms and a laser-supported detonation wave will propagate up the laser incidence axis toward the focal lens (Fig. 7a). This fluid motion creates shearing stresses with the adjacent cooler ambient fluid. The cooler ambient fluid will also begin to move into the back of the plasma region, and the heated fluid will be ejected forward, toward the lens (Figs. 7d–7f). A blast wave begins to move out from the heated region and is initially ellipsoidal in shape due to the asymmetric plasma region. However, the blast wave becomes almost spherical by 15 μs. Baker[26] also observed the spherical blast wave from asymmetric energy sources for larger explosions. A vortex ring structure resides at later times in the heated region due to the asymmetric formation process and the laser-supported detonation wave. The radiation from the bremsstrahlung process subsides by approximately 10 μs and is dependent on the incident radiation energy. Likewise, the strength of the blast wave, magnitude of asymmetry, size of the deposition region, and the strength of the vortex ring depend on the incident energy. These characteristics also depend on the optics of the incident laser, that is, focal length, beam diameter, and beam divergence.

Figures 7a–7i show the time sequence of images of the breakdown from 15 to 300 μs for a laser incidence of 108 mJ/pulse. Each image is an ensemble average of 100 images where the laser sheet for the RS image is phase-locked to the energy deposition laser.

Numerical Initial Condition

The choice of the initial condition for modeling laser energy addition is based on the choice of stage in Fig. 1. We focus on the gasdynamic effects of the laser energy spot; therefore, only the process after stage 4 is within our scope of study. Baker[26] noted that the blast front tends to become spherical in shape with increasing distance from the origin independently of any finite source shape. This is also confirmed in our experiments (Figs. 7a–7d).

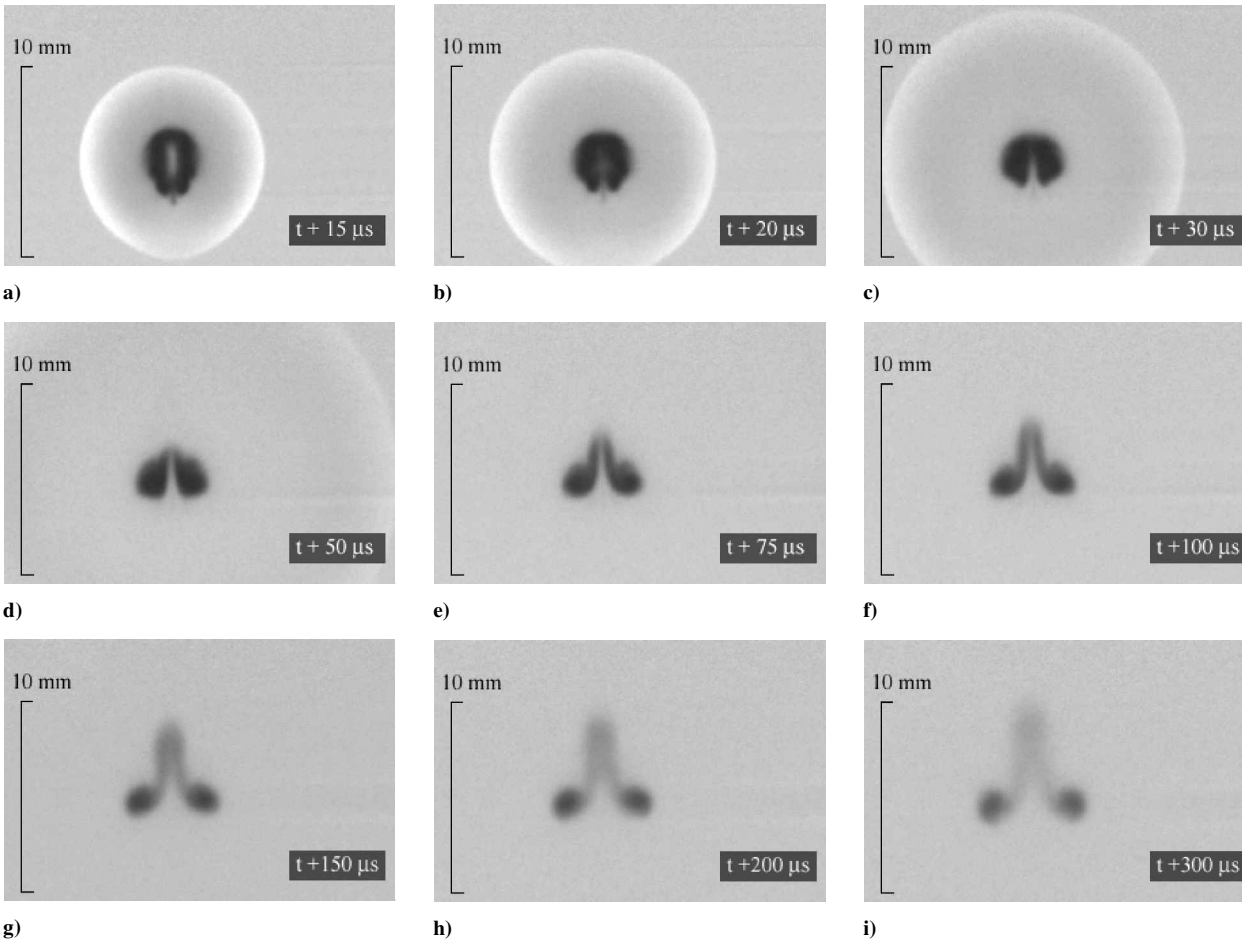

Fig. 7 Flow visualization; time sequence.

Consequently, a spherically symmetric initial temperature distribution is proposed to model the laser energy pulse assuming that the energy is added instantaneously at constant volume (therefore the density is constant) and the gas is ideal. The temperature variation using a Gaussian profile can be written as

$$\Delta T = \Delta T_0 e^{-r^2/r_0^2} \tag{11}$$

where ΔT_0, the peak temperature variation, is determined by the total energy deposited,

$$E = \int_0^{2\pi}\int_0^{\pi}\int_0^{\infty} r^2 \sin\theta \rho_\infty c_v \Delta T \, dr \, d\theta \, d\phi \tag{12}$$

where c_v is the specific heat at constant volume. Substituting Eq. (11) into the preceding equation and integrating it, we obtain

$$\Delta T_0 = E \Big/ \pi^{\frac{3}{2}} r_0^3 \rho_\infty c_v \tag{13}$$

where r_0 is related to the initial radius $R_0 = 0.90$ mm of the laser spot obtained from the laser perturbation focal volume $V_0 = \frac{4}{3}\pi R_0^3$ and set to be $R_0/2$. From Eq. (11), ΔT will reach 2% of ΔT_0 at $r = R_0$.

Computational Results

The ambient condition is $T_\infty = 293$ K, $\rho_\infty = 1.20$ kg/m^3, and freestream velocity $\boldsymbol{U}_\infty = 0$, which is consistent with the experiment. Two different grid spacings ($\Delta r = 0.01$ and 0.02 mm) are used and show 1.3% difference in predicting the profile of shock wave radius vs time in Fig. 8, showing the sufficient grid resolution in the simulation. The grid spacing of $\Delta r = 0.01$ mm was therefore used in all of the simulations.

A blast wave formed by the rapid expansion of the high-pressure and -temperature region propagates into the ambient air. The position of the leading front varying with time for $E = 112$ mJ is shown in Fig. 8. The position of the blast front is determined by locating the maximum pressure along the radial distance from the center of the source. Considering that not all of the laser energy is absorbed and some of the energy is reflected, transmitted, scattered, and emitted by the plasma, the total energy absorbed is assumed to be ϵE. Therefore, Eq. (13) becomes

$$\Delta T_0 = \epsilon E \Big/ \pi^{\frac{3}{2}} r_0^3 \rho_\infty c_v \tag{14}$$

The net energy deposited (ϵE) in the flow affects the flow characteristics. The choice of ϵ is based on the criterion that the standard deviation of the predicted profile of the shock wave radius vs time is within 5% of the experimental fit. The results using $\epsilon = 0.65$ show good agreement with experimental fit given by Adelgren et al. (private communication) for $E = 112$ mJ [$r(t) = 140.692\, t^{0.893} + 2.466 \times 10^{-3}$, where t is in seconds and r in meters] except at very early time instants ($t < 5$ μs) where no experimental data are available. The experimental fit of Adelgren et al. agrees with experiment to within $\pm 5\%$ for $t = 5$ μs to 40 μs.

Taylor[4] and Sedov[6] proposed a similarity law at the early stage of the air explosion, $r(t) = At^{0.4}$, where A is the function of input energy and ambient density when $M_s^2 \gg 1$ (where $M_s = V_s/a_\infty$, and M_s, V_s, and a_∞ are the shock Mach number, shock velocity, and ambient speed of sound, respectively). Jiang et al.[11] utilized this law as the initial condition and they found that the flow showed non-self-simlar behavior in the mid- and far-field regimes where the shock is too weak to follow Taylor's similarity law.

The different behavior in our study compared to Taylor's similarity law is due to the relative weak strength of the shock wave in our case, which is demonstrated in Fig. 8; the Mach number at $t = 5$ μs, which is the first time record in our experiment, is about 1.6 and the shock strength decreases rapidly until it propagates at essentially the speed of sound.

Figures 9–12 show the experimental contour plots for $E = 145$ mJ at $t = 20$ μs. The laser beam is incident from the left. The origin (0, 0) in the x–y plane is the center of the laser spot. For the velocity contours, only the magnitude of the y component is shown. In the experiment, the temperature and pressure were measured and the density was computed from the equation of state for a perfect gas. The experimental uncertainties in the measurement of the pressure, temperature, and velocity are ± 2.33, ± 1.34, and $\pm 3.83\%$, respectively. The central part is blanked out because no experimental data are available there. In the incident direction, the blast wave shows an asymmetric shape due to the directional formation of the plasma, while in the vertical direction, the shape is fairly symmetric and the data is extracted in this direction to compare with the simulation.

Figures 13–16 show the comparison with experiment at $t = 20$ μs for $E = 145$ mJ. The experimental data are extracted along a vertical

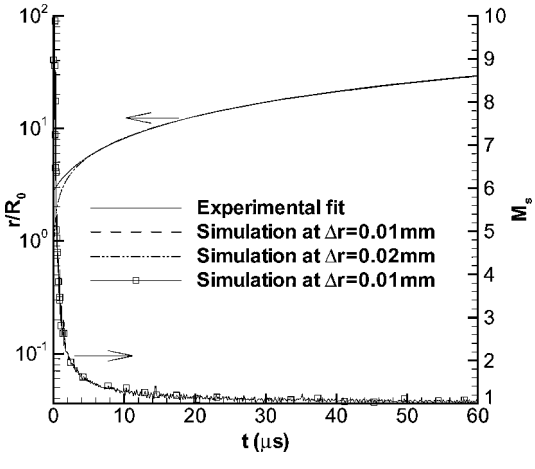

Fig. 8 Shock wave radius and shock Mach number vs time for $E = 112$ mJ.

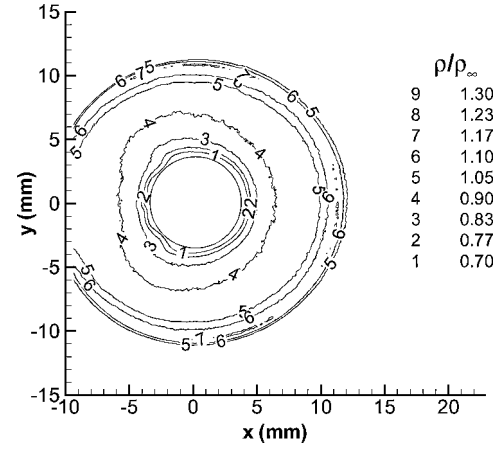

Fig. 9 Density contours at $t = 20$ μs for $E = 145$ mJ.

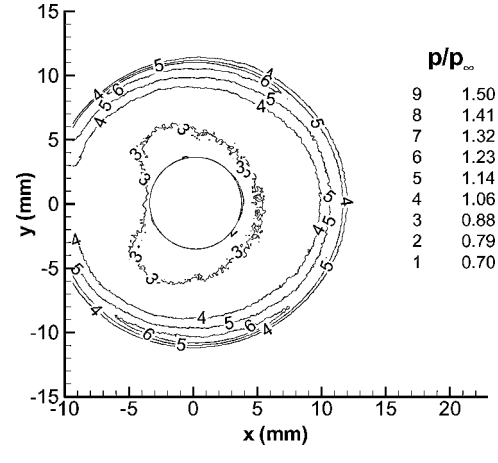

Fig. 10 Pressure contours at $t = 20$ μs for $E = 145$ mJ.

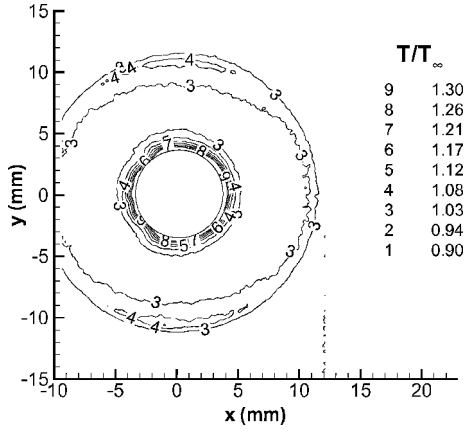

Fig. 11 Temperature contours at $t = 20$ μs for $E = 145$ mJ.

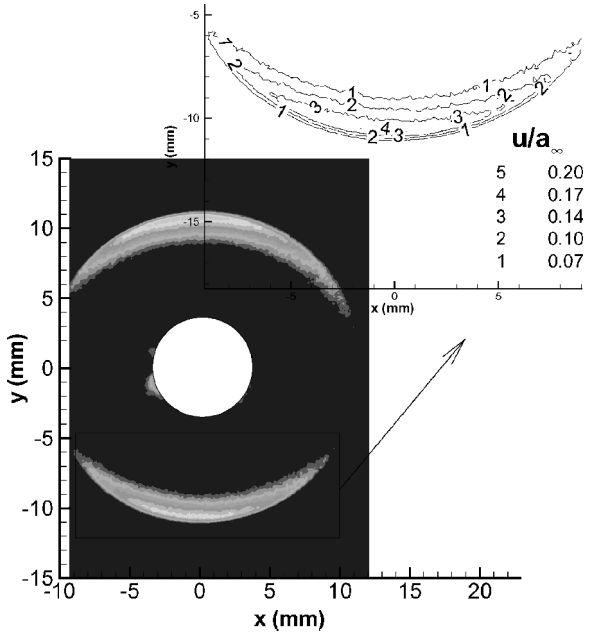

Fig. 12 Velocity contours at $t = 20$ μs for $E = 145$ mJ.

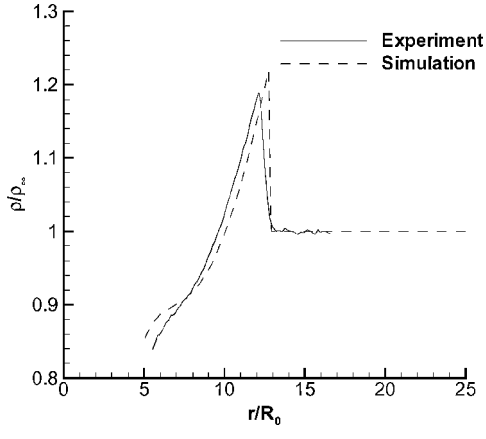

Fig. 13 Density vs radius at $t = 20$ μs for $E = 145$ mJ.

line from $y = 0$ to 15 mm. The assumed absorption coefficient is $\epsilon = 0.5$. Good agreement is achieved for the shock wave position, the magnitude of the change of the flow variables across the shock, and the distribution of flow variables for points with r less than the shock radius and outside the laser spot region. Because the intensity of RS is proportional to the density and the density is very low at the center of the energy spot, the uncertainty increases near the center due to lower signal levels in RS. Also, as mentioned earlier, the RS is

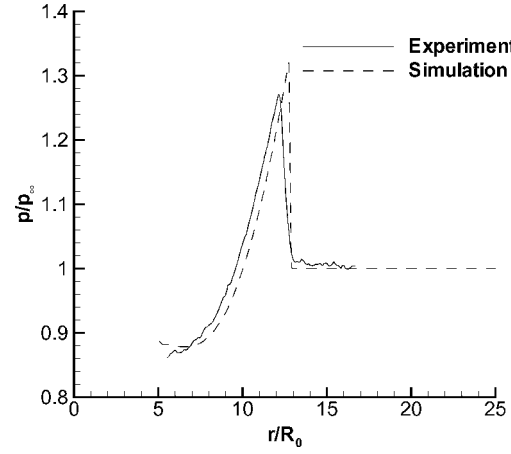

Fig. 14 Pressure vs radius at $t = 20$ μs for $E = 145$ mJ.

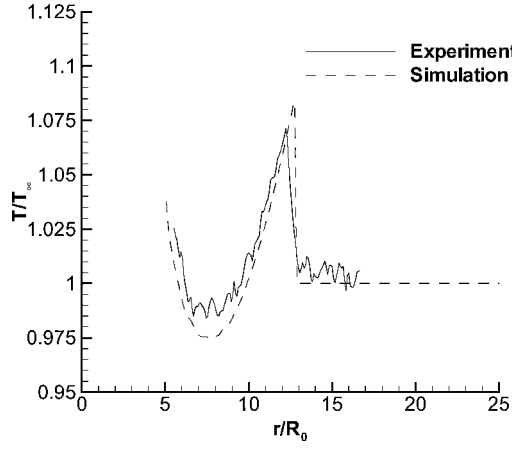

Fig. 15 Temperature vs radius at $t = 20$ μs for $E = 145$ mJ.

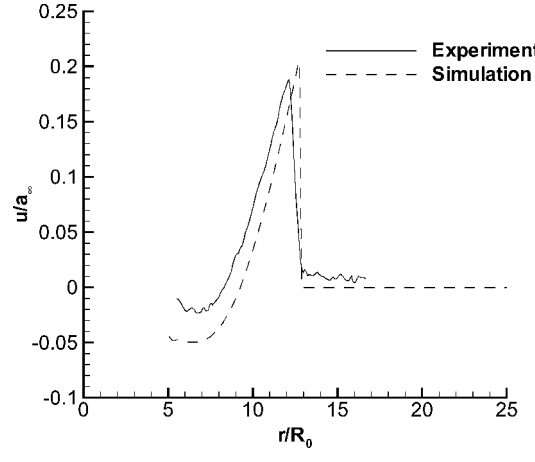

Fig. 16 Velocity vs radius at $t = 20$ μs for $E = 145$ mJ.

dominated by the plasma emission for early time so no experimental information is shown here.

To understand the propagation of the blast wave, we plot the density, pressure, temperature, and velocity distribution along the radius at the different time instants shown in Figs. 17–20. The data for $r/R_0 < 5$ are omitted because the plasma effect in this region is not considered in the simulation. The shock wave propagates through the air along with a decrease in intensity. The attenuation in intensity gradually decreases with time. The expansion fan brings the pressure below ambient. A reversed flow shown in Fig. 20 is formed by the adverse pressure gradient. At the same time, the effect of the expansion fan produces a shock wave moving toward

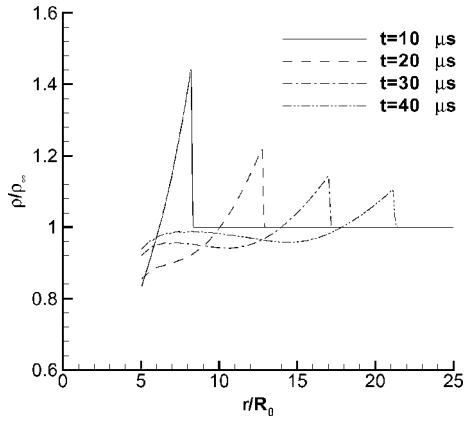

Fig. 17 Density vs radius for $E = 112$ mJ.

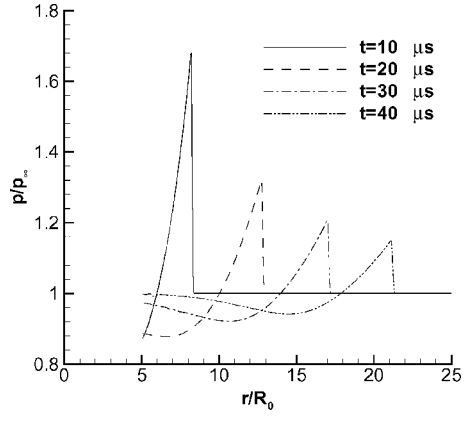

Fig. 18 Pressure vs radius for $E = 112$ mJ.

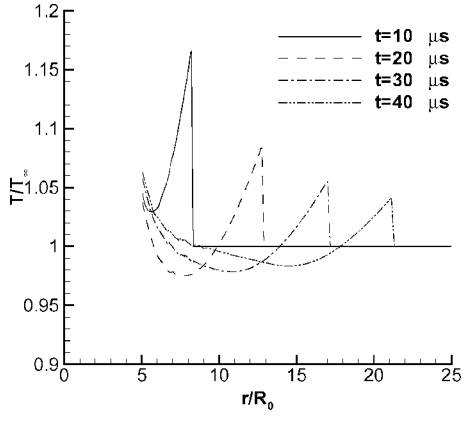

Fig. 19 Temperature vs radius for $E = 112$ mJ.

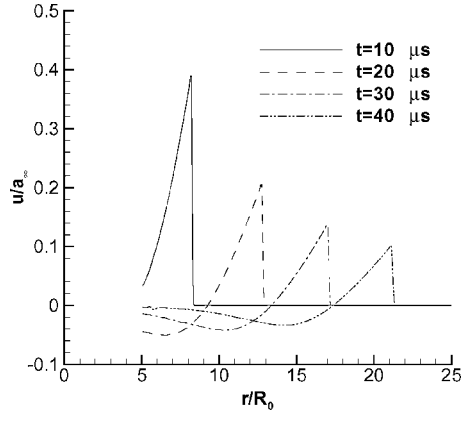

Fig. 20 Velocity vs radius for $E = 112$ mJ.

the origin, causing the pressure recover to the ambient value. The size of the high-temperature region induced by laser energy stays almost constant.

Conclusions

Laser energy deposition in quiescent air has been studied experimentally and numerically. The study is focused on the gasdynamic effect of the laser energy spot. The filtered RS technique successfully captures the shock wave position and provides a good means of visualizing two-dimensional effects of the flowfield. A numerical simulation using a proposed initial temperature distribution to model the energy spot using the Gaussian profile achieves good agreement with experiment for shock radius vs time. The distribution of density, pressure, temperature, and velocity along the radius for $r/R_0 \geq 5$ also agrees well with experiment.

Acknowledgments

This research is supported by the Air Force Office of Scientific Research under Grant F49620-01-1-0368 monitored by John Schmisseur and Steve Walker. All computations were performed at Rutgers University.

References

[1]Maker, P. D., Terhune, R. W., and Savage, C. M., "Optical Third Harmonic Generation," *Quantum Electronics: Proceedings of the 3rd International Congress*, edited by P. Grivet and N. Bloembergen, Vol. 2, Columbia Univ. Press, New York, 1964.

[2]Svetsov, V., Papova, M., Rybakov, V., Artemiev, V., and Medveduk, S., "Jet and Vortex Flow Induced by Anisotropic Blast Wave: Experimental and Computational Study," *Shock Waves*, Vol. 7, 1977, pp. 325–334.

[3]Adelgren, R., Elliott, G., Knight, D., Zheltovodov, A., and Beutner, T., "Energy Deposition in Supersonic Flows," AIAA Paper 2001-0885, Jan. 2001.

[4]Taylor, G. I., "The Formation of a Blast Wave by a Very Intense Explosion: I Theoretical Discussion," *Proceedings of the Royal Society of London*, Vol. 201, 1950, pp. 159–174.

[5]Brode, H. L., "Numerical Solutions of Blast Waves," *Journal of Applied Physics*, Vol. 26, No. 6, 1955, pp. 766–775.

[6]Sedov, L. I., *Similarity and Dimensional Methods in Mechanics*, Academic Press, New York, 1959.

[7]von Neumann, J., "The Point Source Solution," *Collected Works of J. von Neumann*, Vol. 6, Pergamon, Oxford, 1963.

[8]Raizer, Y. P., "Breakdown and Heating of Gasses Under the Influence of a Laser Beam," *Soviet Physics—Uspekhi*, Vol. 8, No. 5, 1966, pp. 650–673.

[9]Morgan, C. C., "Laser-Induced Breakdown of Gases," *Reports on Progress in Physics*, Vol. 38, 1975, pp. 621–665.

[10]Raizer, Y. P., *Gas Discharge Physics*, 2nd ed., Springer-Verlag, New York, 1997.

[11]Jiang, Z., Takayama, K., Moosad, K. P. B., Onodera, O., and Sun, M., "Numerical and Experimental Study of a Micro-Blast Wave Generated by Pulsed-Laser Beam Focusing," *Shock Waves*, Vol. 8, 1998, pp. 337–349.

[12]Steiner, H., Gretler, W., and Hirschler, T., "Numerical Solution for Spherical Laser-Driven Shock Waves," *Shock Waves*, Vol. 8, 1998, pp. 337–349.

[13]Dors, I., Parigger, C., and Lewis, J., "Fluid Dynamic Effects Following Laser-Induced Optical Breakdown," AIAA Paper 2000-0717, Jan. 2000.

[14]Jiang, S. M., Wang, J. S., and Chen, H., "Numerical Study of Spherical Blast-Wave Propagation and Reflection," *Shock Waves*, Vol. 12, 2002, pp. 59–68.

[15]Yan, H., Adelgren, R., Elliott, G., Knight, D., Beutner, T., Ivanov, M., Kudryavtsev, A., and Khotyanovsky, D., "Laser Energy Deposition in Quiescent Air and Intersecting Shocks," *Fourth Workshop on Magneto-Plasma Aerodynamics for Aerospace Applications*, Inst. for High Temperature, Russian Academy of Science, Moscow, 2002.

[16]Bach, G. G., and Lee, J. H. S., "An Analytical Solution for Blast Waves," *AIAA Journal*, Vol. 8, 1970, pp. 271–275.

[17]Miles, R. B., and Lempert, W. R., "Flow Diagnostics in Unseeded Air," AIAA Paper 90-0624, Jan. 1990.

[18]Elliott, G. S., and Beutner, T., "Molecular Filter Based Planar Doppler Velocimetry," *Progress in Aerospace Sciences*, Vol. 35, 1999, pp. 799–845.

[19]Elliott, G. S., Boguszko, M., and Carter, C., "Filtered Rayleigh Scattering: Toward Multiple Property Measurements," AIAA Paper 2001-0301, Jan. 2001.

[20]McCartney, E. J., *Optics of the Atmosphere*, Wiley, New York, 1976.

[21]Forkey, J., "Development and Demonstration of Filtered Rayleigh Scattering—A Laser Based Flow Diagnostic for Planar Measurement of Velocity, Temperature and Pressure," Ph.D Dissertation, Dept. of Mechanical and Aerospace Engineering, Princeton Univ., Princeton, NJ, 1996.

[22]Miles, R. B., Lempert, W. R., and Forkey, J., "Instantaneous Velocity Fields and Background Suppression by Filtered Rayleigh Scattering," AIAA Paper 91-0357, Jan. 1991.

[23]Tenti, G., "On the Kinetic Model Description of Rayleigh–Brillouin Scattering from Molecular Gases," *Canadian Journal of Physics*, Vol. 52, 1994, p. 285.

[24]Boris, J. P., and Book, D. L., "Flux Corrected Transport: I, SHASTA, a Fluid Transport Algorithm That Works," *Journal of Computational Physics*, Vol. 11, 1973, pp. 38–69.

[25]Van Leer, B., "Towards the Ultimate Conservative Difference Scheme. V. A Second Order Sequel to Godunov's Method," *Journal of Computational Physics*, Vol. 32, 1979, pp. 101–136.

[26]Baker, W. E., *Explosions in Air*, Univ. of Texas Press, Austin, TX, 1973.

R. P. Lucht
Associate Editor